Mathematical Biosciences and Engineering

http://www.aimspress.com/journal/mbe

MBE, 23(6): 1743–1767.
DOI: 10.3934/mbe.2026063
Received: 03 April 2026
Revised: 05 May 2026
Accepted: 14 May 2026
Published: 21 May 2026

Research article

Stationary and oscillatory corrosion patterns in a modified Barkley-Leslie-Gower model

Giancarlo Consolo* **and Guglielmo Inferrera**

Department of Mathematical and Computer Sciences, Physical Sciences and Earth Sciences, University of Messina, Viale F. Stagno d'Alcontres 31, 98166 Messina, Italy

* **Correspondence:** Email: gconsolo@unime.it.

Abstract: In this work, we investigated the emergence of stationary and oscillatory patterns in an extended version of the Barkley model for corrosive and passivating species, specifically tailored to describe the initiation stage of localized corrosion at the bottom of fuel tanks. While the proposed model leaves the corrosive reaction unchanged relative to the original formulation, it modifies the kinetics of the passivating species by assuming a Leslie-Gower law with a Holling type II functional response. A rigorous analysis of the dynamical system was first conducted to establish the boundedness of solutions within a positively invariant region and to identify the emergence of Hopf bifurcations. Subsequently, through local stability analysis performed on the full spatial model, the conditions for Turing bifurcations were determined. These analyses highlighted a wide parameter space where Turing and Hopf instabilities coexist, thereby demonstrating the model's capability to trigger stationary and oscillatory corrosion patterns. Numerical investigations in 1D and 2D domains, utilizing direct integration and continuation tools, revealed a large variety of pattern morphologies. Specifically, small computational domains exhibited stripes as well as square and hexagonal holes. In larger domains and across broader parameter ranges, labyrinthine, target, and non-Turing spiral-like patterns also emerged. Beyond validating theoretical predictions, these analyses revealed that patterned branches emerge supercritically in 1D and subcritically in 2D domains, providing a qualitative match with experimental observations. Overall, the proposed framework sheds light on the complex competition between material dissolution and protective film regeneration, serving as a potential support for predictive strategies in the safety management of fuel tanks.

Keywords: activator-inhibitor dynamics; turing and Hopf instabilities; Barkley-Leslie-Gower kinetics; reaction-diffusion systems; corrosion pattern formation

1. Introduction

The transition toward green technologies introduces significant challenges, particularly in the field of biofuel storage. Atmospheric Storage Tanks (ASTs), critical infrastructures for the biofuel industry, are highly exposed to corrosion, which constitutes one of the most relevant threats to their long-term structural integrity [1, 2]. Failure to manage this degradation can lead to the release of hazardous substances, causing severe environmental impacts and posing significant risks to human health. Corrosion refers to the structural or functional degradation of a material resulting from chemical or electrochemical reactions with its surrounding medium [2]. While it may occur uniformly, its most detrimental forms are localized, exemplified by phenomena such as pitting. These attacks occur at discrete sites rather than across the entire surface, leading to the formation of pits, crevices, or other localized defects [3]. Pitting, which involves the development of minute perforations [4], remains a significant issue for tank bottoms. Within the biofuel industry, this vulnerability is heightened by water buildup (due to product impurities, condensation, or rainwater), the presence of particular contaminants, and stagnant environments that promote rapid localized attacks [5–7]. Physicochemical analysis shows that localized corrosion involves a spontaneous breakdown of the passive film that normally protects the metal surface. The ensuing spatial heterogeneity can result in catastrophic structural failure. Consequently, ensuring AST safety relies on regular monitoring, typically via comprehensive inspections every decade [8, 9]. However, these point-in-time thickness readings often fail to accurately identify the peak depth of localized pitting. To improve predictive reliability, researchers have been developing quantitative theoretical models to estimate *pitting evolution* rates relative to exposure duration and environmental shifts [10–14]. Conversely, very little literature [15] focuses on the complex drivers of *pitting initiation*, a gap that we aim to fill.

In particular, when approaching the study of nonlinear chemical dynamics, reaction-diffusion systems offer a powerful framework for describing the competition between metal dissolution (the activator process) and the formation of the oxide film (the inhibitor process). A first attempt to describe the propagation of corrosion waves in excitable media was presented in [13]. In that framework, the original Barkley model [16, 17] was employed to describe the interaction between a fast activator variable, the concentration of corrosive species, and a slow recovery variable, the concentration of the passivating species. However, in its standard form, the model assumed the passivating species to be diffusionless, so that the conditions for diffusion-driven Turing instability, responsible for the emergence of spatial patterns that could mimic the onset of localized corrosion, were never met [18, 19]. A subsequent approach to trigger Turing instability within the framework of the Barkley model was addressed in [15]. In [15], the researchers, by exploiting a dichotomy between different states of the passivating species occurring at a faster time scale, a (nonlinear) cross-diffusion term for this species was derived. Their results demonstrated that Turing patterns can emerge when the cross-diffusion coefficient exceeds a given critical threshold.

In this paper, we prove that by incorporating a more accurate description of the electrochemical interactions occurring at the bottom of fuel tanks, it is possible to generate a rich variety of corrosion patterns in 1D and 2D domains, even when assuming (linear) self-diffusion transport mechanisms for both species. We propose an extended model where the kinetics of the corrosive species remains unchanged from the original Barkley model, while that of the passivating species is governed by a logistic-like Leslie-Gower dynamic with a Holling type II functional response [20, 21]. This modi-

fication captures the limited regenerative capacity of the passive film by introducing a vulnerability threshold, reflecting the behavior of metals in highly aggressive environments. Our objective is to analyze how variations in the carrying capacity of the passive film and the survival threshold of the corrosion density induce a wide range of dynamical regimes, from stationary to oscillatory patterns as well as from supercritical to subcritical ones, thereby providing deeper insights into the mechanisms of localized corrosion.

The manuscript is organized as follows:

In Section 2, we develop the generalized Barkley-Leslie-Gower model and discuss the chemical principles supporting the proposed framework. We determine the system's equilibria and assess their local stability against homogeneous perturbations. Furthermore, we establish a positively invariant region to ensure the global existence and boundedness of solutions of the dynamical system, specifically for the activator-inhibitor configuration. We then focus on identifying the conditions for Hopf and Turing instabilities, which are responsible for the emergence of spatially-uniform time-periodic and time-independent spatially-periodic solutions, respectively.

In Section 3, we are devoted to numerical results. We carry our extensive numerical simulations and build detailed bifurcation diagrams in 1D and 2D domains to illustrate the model's rich patterned dynamics.

Finally, in Section 4, we summarize the major findings of this work and outline potential directions for future research.

2. Materials and methods

The Barkley model [16, 17] is a prominent framework for studying complex spatio-temporal patterns, with a particular focus on propagating waves, such as rotating spirals and turbulence, in excitable media [22]. Its applicability ranges from medical sciences [23] to chemistry [13, 15]. In particular, Batista and coworkers [13] proposed a two-compartment model in the context of the corrosion of metal surfaces driven by an electrolyte solution, such as the one that forms at the bottom of fuel tanks. That model described the interaction between the surface concentration of a corrosive species u, playing the role of a fast activator, and a passivating species v, acting as a slow control variable and assumed to be diffusionless. This framework was used with success to provide a qualitative understanding on the electrochemical dynamics occurring at the electrolyte-metal interface. In its original dimensionless formulation, the Barkley model takes the form:

$$\begin{aligned} \frac{\partial u}{\partial t} - \Delta u &= \delta\, u(1-u)\,(u-(av+b)) \\ \frac{\partial v}{\partial t} &= u - v \end{aligned} \tag{2.1}$$

where Δ denotes the Laplacian operator in the (x, y) plane, whereas the coefficients a, b, and δ are positive parameters, with condition $\delta > 1$ mimicking the fast corrosion rate. Corrosion dynamics is described via an Allee law, where the carrying capacity is normalized to unity and the survival threshold depends linearly on the concentration of the passivating species, $u_{st} = a\,v + b$. Passivating dynamics appears in an oversimplified form through two linear contributions representing a corrosion-induced growth and an intrinsic mortality rate.

Later, the above model was generalized in [15] in a twofold manner to better describe the transport mechanisms of the passivating species. On the one side, a self-diffusion term was included to mimic the flow of the passivating species along its gradient, according to classical Fick's law. On the other side, starting from the chemical consideration that, at a mesoscopic scale, the passivating species may exhibit two states (pure passive and passive film breakdown), in line with the Point Defect Model outlined in [15, 24], and that the corrosive species drives fast transitions between them, an additional cross-diffusion contribution emerged in the resulting limiting governing equation at the macroscale. The extended model then took the form:

$$\begin{aligned} \frac{\partial u}{\partial t} - D_{11}\Delta u &= \delta\, u(1-u)\,(u-(a\,v+b)) \\ \frac{\partial v}{\partial t} - \Delta(D_{22}v + D_{21}uv) &= u - v \end{aligned} \tag{2.2}$$

where D_{11} and D_{22} represent the self-diffusion coefficients of the corrosive and passivating species, respectively, while D_{21} denotes the cross-diffusion coefficient for the passivating one. It is worth noticing that, in model (2.2), the introduction of the cross-diffusive term into the governing equations was crucial to initiate corrosion patterns [15]. Indeed, the mere presence of self-diffusion contributions did not guarantee that the conditions for the diffusion-driven Turing instability would be fulfilled.

However, the above model suffers from a too simplistic description of the passivating dynamics. To address this, we present the following modified version of the Barkley model:

$$\begin{aligned} \frac{\partial u}{\partial t} - D_{11}\Delta u &= \delta\, u(1-u)\,(u-(a\,v+b)) := f(u,v) \\ \frac{\partial v}{\partial t} - D_{22}\Delta v &= v\left(1 - \frac{v}{k_v + d\,(u-u_{th})}\right) := g(u,v) \end{aligned} \tag{2.3}$$

Here, the reaction term for the corrosive species, $f(u,v)$, is left unchanged with respect to the original Barkley formulation. On the contrary, the passivating species is assumed to follow a Leslie-Gower dynamics with a Holling type II functional response [20,21,25], represented by the term $g(u,v)$. Although this approach is typically used in population dynamics, it can significantly enhance the understanding of pitting formation in this context. This formulation aims to reflect the phenomenological observation that the repassivation rate and the stability of the passive film are dynamically influenced by the aggressive environment. To describe these processes in more detail, the reaction term $g(u,v)$ in (2.3) assumes a logistic growth of the passivating species, where the carrying capacity depends linearly on the local concentration of the corrosive species u according to $k(u) = k_v + d\,(u-u_{th})$, where parameters d, k_v, and $u_{th} \in \mathbb{R}^+$. Parameter k_v represents the baseline stability of the film, d scales the response intensity to the corrosive stimulus, and u_{th} defines a critical threshold for the corrosive species below which the passivating action is inhibited or fundamentally altered. Overall, the carrying capacity describes the intrinsic limit for the formation of the passivating species, which defines the maximum thickness of the thermodynamically-stable oxide layer formed on the metal surface. The dependence of the carrying capacity on u also establishes a competition for the active sites where the passivating film can grow. In particular, when chloride ions cause the localized breakdown of the metal surface, the affected site develops an extremely acidic environment (low pH), which prevents the reformation of the protective oxide layer. Moreover, the introduction of a critical threshold u_{th} finds physical and chemical counterparts in the aforementioned Point Defect Model [24]. From the physical viewpoint,

it represents the critical concentration of aggressive ions required to induce an accumulation of cation vacancies at the metal/film interface, a condition that leads to the localized breakdown of the passive layer and the subsequent initiation of the pit. From the chemical standpoint, it models the transition from a stable, passive state to an active corrosive regime. In fact, when u exceeds u_{th}, the interfacial physicochemical conditions facilitate the competitive growth of the inhibitor in an attempt to suppress the autocatalytic growth of the pit, a process effectively captured by the $d(u - u_{th})$ term. Moreover, parameter d quantifies the material's active defensive response, analogous to the anodic growth of oxide films on a metal surface, where the protective layer thickens as the aggressive ion concentration increases. Practically, d can be estimated by exposing the metal tank bottom to varying corrosive environments and measuring the steady-state film thickness via electrochemical impedance spectroscopy, as in [26]. From such experiments, d can be extracted from the $k(u)$ curve mapping the maximum oxide thickness against the corrosive concentration $u > u_{th}$.

Let us also point out that in (2.3), the passivating species simply diffuses according to the classical Fick's law, with a diffusion coefficient D_{22}. Notably, we will prove the model's ability to support stationary and oscillatory patterns even in the absence of cross-diffusion effects.

To preserve the chemical meaning of the quantities involved, the model parameters must meet the following restrictions:

$$av + b < 1 \tag{2.4}$$

to ensure that the Allee threshold for the corrosive species is lower than the carrying capacity and

$$k_v + d\ (u - u_{th}) > 0 \tag{2.5}$$

to ensure the positivity of the carrying capacity of the passivating species. Finally, since the carrying capacity of the corrosive species is set to unity, we impose $u_{th} < 1$.

2.1. Equilibria and linear stability analysis under homogeneous perturbations

In our analysis, we will consider a and d as the major control parameters. These two parameters modulate, respectively, the Allee threshold for the corrosive species and the carrying capacity of the passivating one.

System (2.3) admits the following spatially-homogeneous steady-states $\mathbf{E_i^*} = (u_i^*, v_i^*)$, for $i = 1, ..., 6$, given by:

$$\begin{gathered}\mathbf{E_1^*} = (0,\ k_v - d\,u_{th})\,, \quad \mathbf{E_2^*} = (1,\ k_v + d(1 - u_{th}))\,, \quad \mathbf{E_3^*} = \left(\frac{b + a(k_v - d\,u_{th})}{1 - ad},\ \frac{bd + k_v - d\,u_{th}}{1 - ad}\right) \\ \mathbf{E_4^*} = (0,\ 0), \qquad \mathbf{E_5^*} = (1,\ 0), \qquad \mathbf{E_6^*} = (b,\ 0).\end{gathered} \tag{2.6}$$

Equilibrium $\mathbf{E_1^*}$ exists for $d < k_v/u_{th}$, and the requirement (2.5) is fulfilled under the same restriction, whereas condition (2.4) is satisfied in the following cases:

$$\text{if } b < 1 \ \rightarrow \quad \tfrac{k_v}{u_{th}} + \tfrac{b-1}{a\,u_{th}} < d < \tfrac{k_v}{u_{th}} \tag{2.7}$$

$$\text{if } b \geq 1 \ \rightarrow \quad \text{never} \tag{2.8}$$

Regarding $\mathbf{E_2^*}$, it always exists and fulfils condition (2.5), while (2.4) holds for $d < (1 - b - a\,k_v)\,/\big[a\,(1 - u_{th})\big]$.

As for the coexistence state $\mathbf{E}^*_{\mathbf{3}}$, it exists and fulfils conditions (2.4) and (2.5) in the following cases:

$$\text{if } a\,d < 1 \quad \rightarrow \quad d < \min\left\{\frac{k_v}{u_{th}-b}, \frac{b+a\,k_v}{a\,u_{th}}, \frac{1}{a}, \frac{1-b-a\,k_v}{a(1-u_{th})}\right\} \equiv \hat{d}(a) \tag{2.9}$$

$$\text{if } a\,d > 1 \quad \rightarrow \quad d > \max\left\{\frac{k_v}{u_{th}-b}, \frac{b+a\,k_v}{a\,u_{th}}, \frac{1}{a}, \frac{1-b-a\,k_v}{a(1-u_{th})}\right\} \equiv \tilde{d}(a) \tag{2.10}$$

The remaining equilibria $\mathbf{E}^*_{\mathbf{4,5,6}}$ exist for any model parameter, fulfilling (2.4) for $b < 1$ and (2.5) for $k_v - d\,u_{th} > 0$, $k_v - d\,(1-u_{th}) > 0$, and $k_v - d\,(b-u_{th}) > 0$, respectively.

To address the linear stability analysis on these steady states, let us first recast the governing model (2.3) as:

$$\underbrace{\frac{\partial}{\partial t}\begin{pmatrix} u \\ v \end{pmatrix}}_{\mathbf{E}} = \underbrace{\begin{pmatrix} D_{11} & 0 \\ 0 & D_{22} \end{pmatrix}}_{\mathcal{D}}\begin{pmatrix} \Delta u \\ \Delta v \end{pmatrix} + \underbrace{\begin{pmatrix} \delta u(1-u)\,(u-(a\,v+b)) \\ v\left(1-\frac{v}{k_v+d\,(u-u_{th})}\right) \end{pmatrix}}_{\mathbf{R}(\mathbf{E})} \tag{2.11}$$

and introduce a small perturbation around $\mathbf{E}^*$ in the form of a simple Fourier mode

$$\mathbf{E} = \mathbf{E}^* + \hat{\mathbf{E}}\exp\left(\lambda t + \mathrm{i}\boldsymbol{\kappa}\cdot\mathbf{x}\right), \tag{2.12}$$

where λ and $\boldsymbol{\kappa} = (\kappa_1, \kappa_2)$ represent the growth factor and the wavevector of the perturbation, respectively, and $\mathbf{x} = (x_1, x_2)$.

The local stability character of each steady state under homogeneous perturbations is then addressed by considering the linearized problem in the absence of spatial disturbances ($\boldsymbol{\kappa} = \mathbf{0}$)

$$\left(J\left(\mathbf{E}^*\right) - \lambda\mathcal{I}\right)\hat{\mathbf{E}} = \mathbf{0} \tag{2.13}$$

which leads to the characteristic equation

$$\lambda^2 - \lambda\,\mathrm{tr}J(\mathbf{E}^*) + \mathrm{det}J(\mathbf{E}^*) = 0. \tag{2.14}$$

In (2.13) and (2.14), $\mathcal{I}$ is the 2×2 identity matrix and J represents the Jacobian matrix:

$$J(\mathbf{E}^*) = \begin{pmatrix} f^*_u & f^*_v \\ g^*_u & g^*_v \end{pmatrix}, \tag{2.15}$$

where the subscripts denote the partial derivatives with respect to the indicated variable, and the asterisks indicate that the functions are evaluated at $\mathbf{E}^*$. As known, an equilibrium is locally stable under spatially-homogeneous perturbations iff $\mathrm{tr}J(\mathbf{E}^*) < 0$ and $\mathrm{det}J(\mathbf{E}^*) > 0$.

In the model proposed here, the partial derivatives take the form:

$$\begin{gathered} f^*_u = \delta\left[2\,u^*\,(b+1) + a\,v^*\,(2\,u^*-1) - b - 3\,u^{*2}\right], \quad f^*_v = \delta\,a\,u^*\,(u^*-1) \\ g^*_u = \frac{d\,v^{*2}}{\left(\widetilde{k_v} + d\,u^*\right)^2}, \quad g^*_v = 1 - \frac{2v^*}{\widetilde{k_v} + d\,u^*} \end{gathered} \tag{2.16}$$

where we have set $\widetilde{k_v} = k_v - d\,u_{th}$.

By combining (2.16) with (2.6), under the assumption that conditions (2.4) and (2.5) are met, straightforward calculations yield the following conclusions:

Equilibrium	$\mathrm{tr}(J(\mathbf{E}^*))$	$\det(J(\mathbf{E}^*))$	Local stability ($\boldsymbol{\kappa} = \mathbf{0}$)
$\mathbf{E}_1^*$	$-\delta(b + a\widetilde{k}_v) - 1 < 0$	$\delta(b + a\widetilde{k}_v) > 0$	always
$\mathbf{E}_2^*$	$\delta\left(b - 1 + a(\widetilde{k}_v + d)\right) - 1 < 0$	$-\delta\left(b - 1 + a(\widetilde{k}_v + d)\right) > 0$	always
$\mathbf{E}_3^*$	$f_u^*\left(\mathbf{E}_3^*\right) - 1 < 0$ for $\tilde{d}(a) < d < d_H(a)$	$f_u^*\left(\mathbf{E}_3^*\right)(ad - 1) > 0$ for $d > \tilde{d}(a)$	for $\tilde{d}(a) < d < d_H(a)$
$\mathbf{E}_4^*$	$1 - \delta\, b < 0$ for $b < 1/\delta$	$-\delta\, b < 0$	never
$\mathbf{E}_5^*$	$1 + \delta\,(b - 1) < 0$ for $b < 1 - 1/\delta < 1$	$\delta\,(b - 1) > 0$ for $b > 1$	never
$\mathbf{E}_6^*$	$1 + \delta\, b(1 - b) < 0$ for $b > \frac{1}{2}\left(1 + \sqrt{1 + \frac{4}{\delta}}\right) > 1$	$\delta\, b(1 - b) > 0$ for $b < 1$	never

where

$$f_u^*\left(\mathbf{E}_{\mathbf{3}}^*\right) = \frac{\delta\left[b + a\left(k_v - d\,u_{th}\right)\right]\left[1 - b - a\left(k_v + d\left(1 - u_{th}\right)\right)\right]}{(1 - ad)^2}, \tag{2.17}$$

$$d_H(a) = \frac{\eta(a) + \left(u_{th} - b - a\,k_v\right)\sqrt{\delta\,(\delta - 4)}}{2\,a\left[\delta\,u_{th}\left(1 - u_{th}\right) - 1\right]}, \tag{2.18}$$

with

$$\eta(a) = \delta\left[b + a\,k_v + u_{th}\left(1 - 2\,(b + a\,k_v)\right)\right] - 2, \tag{2.19}$$

under the restriction $\delta > 4$.

The above results indicate that only the steady states $\mathbf{E}_1^*$, $\mathbf{E}_2^*$, and $\mathbf{E}_3^*$ can be locally stable under homogeneous perturbations. However, the only coexistence state $\mathbf{E}_3^*$ may exhibit the typical behavior of an activator-inhibitor system characterized by $f_u^* > 0$ and $g_v^* < 0$ [19]. In fact, keeping in mind that $g_v^*\left(\mathbf{E}_3^*\right) = -1 < 0$, the conditions $f_u^*\left(\mathbf{E}_3^*\right) > 0$ and $\det(J(\mathbf{E}_{\mathbf{3}}{}^*)) = f_u^*\left(\mathbf{E}_3^*\right)(ad - 1) > 0$ are fulfilled for $d > \tilde{d}(a)$, which rules out case (2.9). On the contrary, the other stable states are characterized by $f_u^*\left(\mathbf{E}_{1,2}^*\right) < 0$ and $g_v^*\left(\mathbf{E}_{1,2}^*\right) < 0$.

For all the above reasons, and considering our interest in detecting the occurrence of meaningful temporal and/or spatial oscillations about non-null states, going forward, we focus our attention on equilibrium $\mathbf{E}_3^*$ only.

2.1.1. Positively-invariant region

Let us prove that the dynamical system $\mathbf{E}_t = \mathbf{R}(\mathbf{E})$ admits a positively invariant region Ω in the phase plane (u, v) about the state $\mathbf{E}_3^* = (u_3^*, v_3^*)$. In particular, it can be demonstrated that there exists a convex bounded region of trapezoidal shape such that, if the initial datum lies in Ω, then the solution $(u(t), v(t))$ lies in Ω for $\forall (u, v) \in \Omega$ and $\forall t > 0$ [27].

Theorem 2.1. *Let* $\Omega = \left\{(u,v) : \alpha \le u \le 1 \ \wedge \ 0 \le v \le \sigma\, u + \psi\right\}$, *where*

$$\alpha = \frac{d\, u_{th} - k_v}{d}, \qquad \sigma = \frac{a\gamma\beta - \alpha + b}{a(1-\alpha)}, \qquad \psi = \frac{\alpha - b - a\alpha\gamma\beta}{a(1-\alpha)}, \qquad \beta = k_v + d(1-u_{th}), \qquad \gamma \ge 1. \tag{2.20}$$

If the model parameters satisfy restriction (2.10) *with*

$$\delta(\alpha - b - a\gamma\beta)\, u(1-u)\left[u - a(\sigma\, u + \psi) - b\right] + a(1-\alpha)(\sigma\, u + \psi)\left[1 - \frac{\sigma\, u + \psi}{k_v + d(u - u_{th})}\right] \le 0 \tag{2.21}$$

for $u \in [\alpha, 1]$, *then* Ω *is a positively invariant region for the dynamical system* $\mathbf{E}_t = \mathbf{R}(\mathbf{E})$.

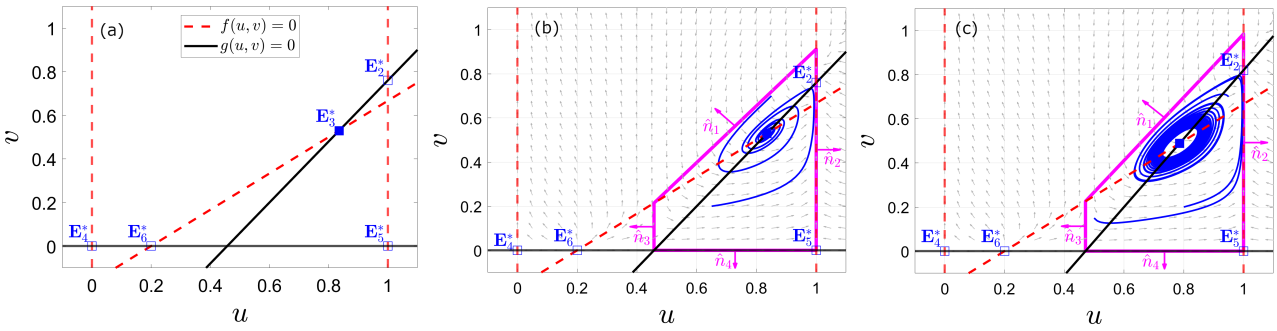

Figure 1. (a) Nullclines of the dynamical system $\mathbf{E}_t = \mathbf{R}(\mathbf{E})$ with equilibria: filled squares (stable) and empty squares (unstable). (b),(c) Phase portraits showing the existence of a positively-invariant region (the magenta trapezoid). In panel (c), the existence of a limit cycle is also pointed out. Common parameters (satisfying restrictions (2.10) and (2.21)): $u_{th} = 0.6$, $b = 0.2$, $k_v = 0.2$, $a = 1.2$, $\delta = 6$, $\gamma = 1.2$. In (b), we use $d = 1.4$, which falls into the range $\tilde{d} < d < d_H$, while in (c), $d = 1.55$ corresponds to $d > d_H$.

Proof. Let us consider the trapezoidal region of the phase plane delimited by the four straight lines $\Omega = \left\{(u,v) : \alpha \le u \le 1 \ \wedge \ 0 \le v \le \sigma\, u + \psi\right\}$ and characterized by the outer normal unit vectors $\hat{n}_j$, with $j = 1, .., 4$, depicted in Figure 1(b). To establish that Ω is a positively invariant region for the dynamical system $\mathbf{E}_t = \mathbf{R}(\mathbf{E})$, with reaction terms $\mathbf{R} = (f(u,v), g(u,v))^T$ defined in (2.11), let us prove that $\langle \mathbf{R}(t;\bar{\mathbf{E}}), \hat{n}\rangle \le 0 \quad \forall t \in \mathbb{R}^+, \bar{\mathbf{E}} \in \partial\Omega, \hat{n} \in \mathcal{N}_\Omega$, under the assignment (2.20). Here, $\langle , \rangle$ denotes the scalar product, and $\mathcal{N}_\Omega$ represents the set of all the outer normal unit vectors to the boundaries of region Ω.

- On the oblique boundary, $\hat{n}_1 = \left(\frac{\alpha-b-a\gamma\beta}{\sqrt{(\alpha-b-a\gamma\beta)^2+a^2(1-\alpha)^2}}, \frac{a(1-\alpha)}{\sqrt{(\alpha-b-a\gamma\beta)^2+a^2(1-\alpha)^2}}\right)^T$ is the outer normal, $\bar{\mathbf{E}} = (u, \sigma\, u + \psi)$ and $u \in [\alpha, 1]$. Thus, $\langle \mathbf{R}(t;\bar{\mathbf{E}}), \hat{n}_1\rangle = \delta(\alpha - b - a\gamma\beta)\, u(1-u)\left[u - a(\sigma\, u + \psi) - b\right] + a(1-\alpha)(\sigma\, u + \psi)\left[1 - \frac{\sigma\, u+\psi}{k_v + d(u-u_{th})}\right] \le 0$, which is fulfilled for suitable choices of the model parameters.
- On the right boundary, $\hat{n}_2 = (1,0)^T$ is the outer normal, $\bar{\mathbf{E}} = (1, v)$ and $v \in [0, \sigma + \psi]$. Thus, $\langle \mathbf{R}(t;\bar{\mathbf{E}}), \hat{n}_2\rangle = 0$.
- On the lower boundary, $\hat{n}_3 = (0,-1)^T$ is the outer normal, $\bar{\mathbf{E}} = (u, 0)$ and $u \in [\alpha, 1]$. Thus, $\langle \mathbf{R}(t;\bar{\mathbf{E}}), \hat{n}_3\rangle = 0$.

- On the left boundary, $\hat{n}_4 = (0,1)^T$ is the outer normal, $\bar{\mathbf{E}} = (\alpha, v)$ and $v \in [0, \frac{\alpha-b}{a}]$. Thus, $\langle \mathbf{R}(t;\bar{\mathbf{E}}), \hat{n}_4 \rangle = -\delta\alpha(1-\alpha)[\alpha - b - a\,v] \leq 0$ which is fulfilled being $\alpha < 1$ and $v \leq \frac{\alpha-b}{a}$.

Therefore, Ω is a positively invariant region for the dynamical system $\mathbf{E}_t = \mathbf{R}(\mathbf{E})$ under the assignements (2.20).

2.1.2. Hopf bifurcation

Let us now prove the occurrence of Hopf bifurcations in the proposed dynamical system $\mathbf{E}_t = \mathbf{R}(\mathbf{E})$ and, in particular, let us inspect the possibility that the steady state $\mathbf{E}_3^*$ undergoes a transition toward a spatially-uniform periodic-in-time solution. To this aim, the characteristic equation (2.14) should admit a pair of purely imaginary conjugate roots $\lambda = \pm i\omega$, and the transversality condition $\frac{\mathrm{dRe}\lambda}{\mathrm{d}\,d}\Big|_{d=d_{cr}} \neq 0$ must be fulfilled at the critical value of the control parameter $d = d_{cr}$ at which such a bifurcation occurs.

It can be proved that the occurrence of a pair of purely imaginary conjugate roots in the characteristic equation is equivalent to requiring that $\mathrm{tr}(J(\mathbf{E_3}^*)) = 0$, which occurs at $d_{cr}(a) \equiv d_H(a)$ given in (2.18). Moreover,

$$\left.\frac{\mathrm{d}\,\mathrm{Re}\lambda}{\mathrm{d}\,d}\right|_{d=d_H} = a\,(u_{th} - b - a\,k_v)\,\sqrt{\delta\,(\delta-4)} \neq 0 \tag{2.22}$$

which is fulfilled under the restrictions $u_{th} \neq b + a\,k_v$ and $\delta > 4$. This result indicates that, with increasing control parameter d, the steady state $\mathbf{E_3}^*$ loses stability at $d = d_H$ through a Hopf bifurcation and generates a limit cycle with period:

$$T = 2\pi\sqrt{\frac{a\,d_H - 1}{\delta\Big[b + a\,(k_v - d_H\,u_{th})\Big]\Big[1 - b - a[d_H(1-u_{th}) + k_v]\Big]}} \tag{2.23}$$

2.2. Linear stability analysis under non-homogeneous perturbations

Let us linearize model (2.11) using (2.12) in the presence of spatial ($\boldsymbol{\kappa} \neq \mathbf{0}$) disturbances as:

$$\left(\lambda\mathcal{I} - J\,(\mathbf{E_3^*}) + \mathcal{D}\,\kappa^2\right)\hat{\mathbf{E}} = \mathbf{0} \tag{2.24}$$

with κ^2 as the square modulus of the wavevector. By expanding the characteristic equation (2.24), it follows that

$$\lambda^2 - \lambda\,m(\kappa^2) + h(\kappa^2) = 0, \tag{2.25}$$

where

$$m(\kappa^2) = \mathrm{tr}\,(J\,(\mathbf{E_3^*})) - \kappa^2(D_{11} + D_{22}), \tag{2.26a}$$

$$h(\kappa^2) = D_{11}D_{22}\,\kappa^4 - q\,\kappa^2 + \det\,(J\,(\mathbf{E_3^*}))\,, \tag{2.26b}$$

with $q = D_{22}f_u^* + D_{11}g_v^*$. It can be noticed that, being $D_{11} > 0$, $D_{22} > 0$ and the condition $\mathrm{tr}\left(J\left(\mathbf{E_3^*}\right)\right) < 0$ holds for the local stability against uniform perturbations, it immediately follows that $m(\kappa^2) < 0$ in (2.26a) is fulfilled for any value of model parameters and wavenumber. Therefore, the stability of the equilibria under non-homogeneous perturbations is determined only by the sign of function $h(\kappa^2)$ defined in (2.26b). Since it is also required that $\det\left(J\left(\mathbf{E_3^*}\right)\right) > 0$, the characteristic equation (2.25) admits eigenvalues with negative real part for any wavenumber κ, and thus the steady state $\mathbf{E_3^*}$ is locally

stable with respect to homogeneous and non-homogeneous perturbations if and only if the following conditions

$$\begin{cases} f_u^*\left(\mathbf{E}_\mathbf{3}^*\right) - 1 < 0, \\ f_u^*\left(\mathbf{E}_\mathbf{3}^*\right)(ad-1) > 0, \\ \left(f_u^* D_{22} + D_{11}\right)^2 - 4adD_{11}D_{22}f_u^*\left(\mathbf{E}_\mathbf{3}^*\right) < 0, \end{cases} \tag{2.27}$$

are fulfilled. These lead to

$$\begin{cases} \tilde{d} < d < d_H \\ \rho_5 d^5 + \rho_4 d^4 + \rho_3 d^3 + \rho_2 d^2 + \rho_1 d + \rho_0 < 0 \end{cases} \tag{2.28}$$

where $f_u^*\left(\mathbf{E}_\mathbf{3}^*\right)$, $\tilde{d}$, and d_H are defined in (2.17), (2.10), and (2.18), respectively, while

$$\rho_0 = \left[D_{11} + D_{22}\,\delta(1-b-ak_v)(b+ak_v)\right]^2, \tag{2.29}$$

$$\begin{aligned} \rho_1 = {} & 2a\Big\{-2D_{11}^2 - D_{22}^2\delta^2(1-b-ak_v)(b+ak_v)\Big[u_{th} + (1-u_{th})(b+a\,k_v)\Big] + \\ & - D_{11}D_{22}\delta\Big[(1-u_{th})(b+a\,k_v) + u_{th}(1-b-a\,k_v) + 4(b+a\,k_v)(1-b-a\,k_v)\Big], \end{aligned} \tag{2.30}$$

$$\begin{aligned} \rho_2 = {} & a^2\Big\{6D_{11}^2 + \\ & 2D_{11}D_{22}\delta\Big[u_{th}(1-u_{th}) + 4\left[(1-u_{th})(b+a\,k_v) + u_{th}(1-b-a\,k_v) + 5(b+a\,k_v)(1-b-a\,k_v)\right]\Big] + \\ & D_{22}^2\delta^2\left[(b+a\,k_v)(1-u_{th})\left[(b+a\,k_v)(1-u_{th}) + 4u_{th}(1-u_{th})\right] + u_{th}^2(1-b-a\,k_v)\right]\Big\}, \end{aligned} \tag{2.31}$$

$$\begin{aligned} \rho_3 = {} & 2a^3\Big\{-2D_{11}^2 - D_{22}^2\,\delta^2\,u_{th}(1-u_{th})(1-b-a\,k_v)[u_{th} + (1-2u_{th})(b+a\,k_v)] + \\ & - D_{11}D_{22}\delta\left[(b+a\,k_v)\left(2(1-b-a\,k_v) + 5(1-2u_{th})\right) + u_{th}(9-4u_{th})\right]\Big\}, \end{aligned} \tag{2.32}$$

$$\rho_4 = a^4\Big\{D_{11}^2 + D_{22}^2\,\delta^2\,u_{th}^2\,(u_{th}-1)^2 + 2D_{11}D_{22}\delta\left[2\,(1-2\,u_{th})(b+a\,k_v) + u_{th}\,(7-5u_{th})\,\right]\Big\}, \tag{2.33}$$

$$\rho_5 = 4a^5\,D_{11}D_{22}\,\delta\,u_{th}(u_{th}-1). \tag{2.34}$$

2.2.1. Turing bifurcation

As known, the presence of diffusion terms in a reaction-diffusion system may lead to the loss of stability of a spatially-homogeneous steady state and the emergence of spatial patterns [15, 18, 19, 28–30]. To inspect the possibility of triggering Turing-type diffusion-driven instabilities about $\mathbf{E}_\mathbf{3}^*$, it is required that $\mathrm{Re}\{\lambda(\kappa)\} > 0$ for some $\kappa \neq 0$. By inspecting (2.25) and (2.26b), the only possibility for this to occur is that the function $h(\kappa^2) < 0$ requires $q > 0$ violating $(2.27)_3$. Moreover, as known, it is also required that, as the control parameter is varied, the transition of the real part of the most unstable eigenvalue from negative to positive should occur via a maximum [19]. By denoting as d_T and κ_T, respectively, the critical values of the control parameter and wavenumber at which such a transition occurs, we end up with

$$\begin{cases} \left[f_u^* D_{22} + g_v^* D_{11}\right]^2 - 4D_{11}D_{22}(f_u^* g_v^* - f_v^* g_u^*) = 0, \\ \kappa_T^2 = \left.\dfrac{D_{22}f_u^* + D_{11}g_v^*}{2D_{11}D_{22}}\right|_{d=d_T}, \end{cases} \tag{2.35}$$

under the restriction $q > 0$. In (2.35), the first equation represents the Turing bifurcation locus, which defines implicitly the critical value d_T. Since we are interested in evaluating the possibility of generating corrosion patterns around the steady-states $\mathbf{E}_3^*$, the Turing locus specializes as follows:

$$\rho_5 d^5 + \rho_4 d^4 + \rho_3 d^3 + \rho_2 d^2 + \rho_1 d + \rho_0 = 0 \tag{2.36}$$

where ρ_i $(i = 1, ..., 5)$, defined in (2.29)–(2.34), whereas the critical wavenumber takes the form:

$$\kappa_T^2 = \sqrt{\delta \frac{\left[b + a\,(k_v - d_T\,u_{th})\right]\left[1 - b - a\,(k_v + d_T(1 - u_{th}))\right]}{(ad - 1)D_{11}D_{22}}} \tag{2.37}$$

The nonlinear and nontrivial dependences of the Turing locus on the control parameters prevent any other analytical investigation. Therefore, additional information are extracted by numerical investigation. In Figure 2, we summarize the theoretical predictions on the existence and the stability of the coexistence state $\mathbf{E}_3^*$ against homogeneous and non-homogeneous perturbations. Here, the solid red line depicts the locus $d = \tilde{d}(a)$, given in (2.10), below which the steady state $\mathbf{E}_3^*$ does not exist and does not fulfil conditions (2.4) and (2.5) (region I). The dashed green line denotes the Turing locus $d = d_T(a)$, given in (2.36), so that region II ($\tilde{d} < d < d_T$) represents the region where $\mathbf{E}_3^*$ is locally stable with respect to spatially-homogeneous and non-homogeneous perturbations. The dash-dotted magenta line is the Hopf locus $d = \tilde{d}(a)$ given in (2.18), and region III ($d_T < d < d_H$) thus identifies the Turing pattern forming region, namely the portion of the parameter plane where $\mathbf{E}_3^*$ is locally stable with respect to spatially-homogeneous perturbations but is destabilized by non-homogeneous ones. Finally, in region IV ($d > d_H$), the equilibrium loses stability via Hopf bifurcation and Turing and Hopf instabilities coexist.

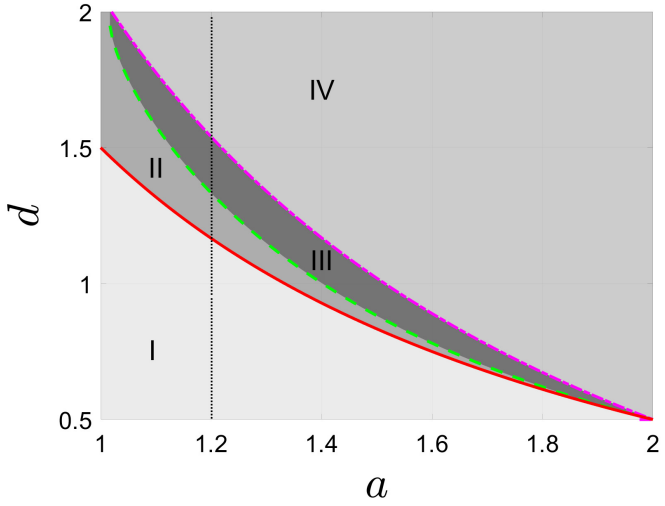

Figure 2. Existence and local stability of equilibrium $\mathbf{E}_3^*$ in the (a, d) parameter plane. Solid red, dashed green, and dash-dotted magenta lines are representative of: $d = \tilde{d}(a)$ (existence locus), $d = d_T(a)$ (Turing locus), and $d = d_H(a)$ (Hopf locus), respectively. Parameters: $u_{th} = 0.6$, $b = 0.2$, $\delta = 6$, $k_v = 0.2$, $D_{11} = 0.1$, and $D_{22} = 0.6$. The dotted vertical line $a = 1.2$ is used as a guide to the eye to denote the continuation analyses depicted in Figures 3 and 6.

3. Numerical results

In this Section, we will address numerical investigations with a twofold goal. On the one hand, we build the bifurcation diagram to validate the existence of Turing and Hopf bifurcations as well as to explore their stability. On the other hand, we integrate the governing system numerically to observe whether the formation and the spatio-temporal evolution of the resulting patterned solutions is consistent with our analytical predictions. Analyses will be performed in 1D and 2D domains.

3.1. Analyses in 1D domains

Figure 3 displays the 1D bifurcation diagram computed by means of the continuation tool *pde2path* [31–33], where stable (unstable) branches are denoted by thick (thin) lines. To build this diagram and enable the possibility to observe all the above instabilities, d is taken as the main control parameter, and the coefficient is set to $a = 1.2$ (see the dotted line in Figure 2), while all the other parameters are kept fixed at the values reported in the caption of Figure 2. The computational domain is set to $x \in [-10, 10]$, and Neumann boundary conditions have been considered. Moreover, we verify that condition (2.21) holds for all numerical examples reported in this paper. The diagram reports the conductive branch in black, representing the zero-amplitude patterned mode, which becomes unstable at $d = d_T = 1.33$, in line with the theoretical prediction given in Eq (2.36). At this critical value of the control parameter, the uniform steady state $\mathbf{E}_3^*$ loses its stability, and a primary, supercritical, branch of stable patterned state originates (see the thick blue curve in Figure 3). Then, other secondary patterned branches emerge from the conductive state for larger values of the control parameter. It can be checked that these branches exhibit re-stabilizing bifurcations, typical of the phenomenon of Eckhaus instability of stationary patterns [34–36].

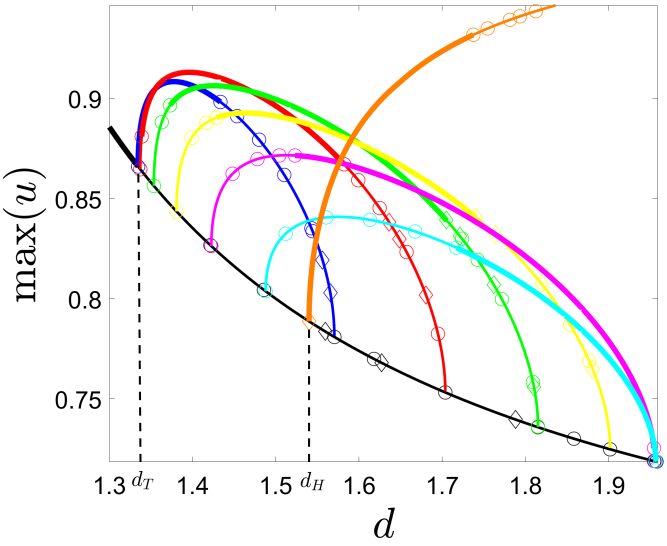

Figure 3. Bifurcation diagram for the 1D model computed with the continuation tool pde2path on the domain $x \in [-10, 10]$, with d as the control parameter and $a = 1.2$. All the other parameters are the same as in Figure 2. Here, stable (unstable) branches are denoted by thick (thin) lines.

At $d = d_H = 1.54$, a supercritical Hopf bifurcation is detected (orange thick line), agreeing with the prediction reported in Section 2.1.2 (see also Eq (2.18) for the explicit expression of the Hopf threshold). Interestingly, the inspection of the bifurcation diagram also reveals a range of the control parameter ($1.54 \leq d \leq 1.74$) where stable Turing and Hopf branches coexist. Therefore, it is expected that the proposed model could also admit oscillating-in-time spatially-periodic solutions.

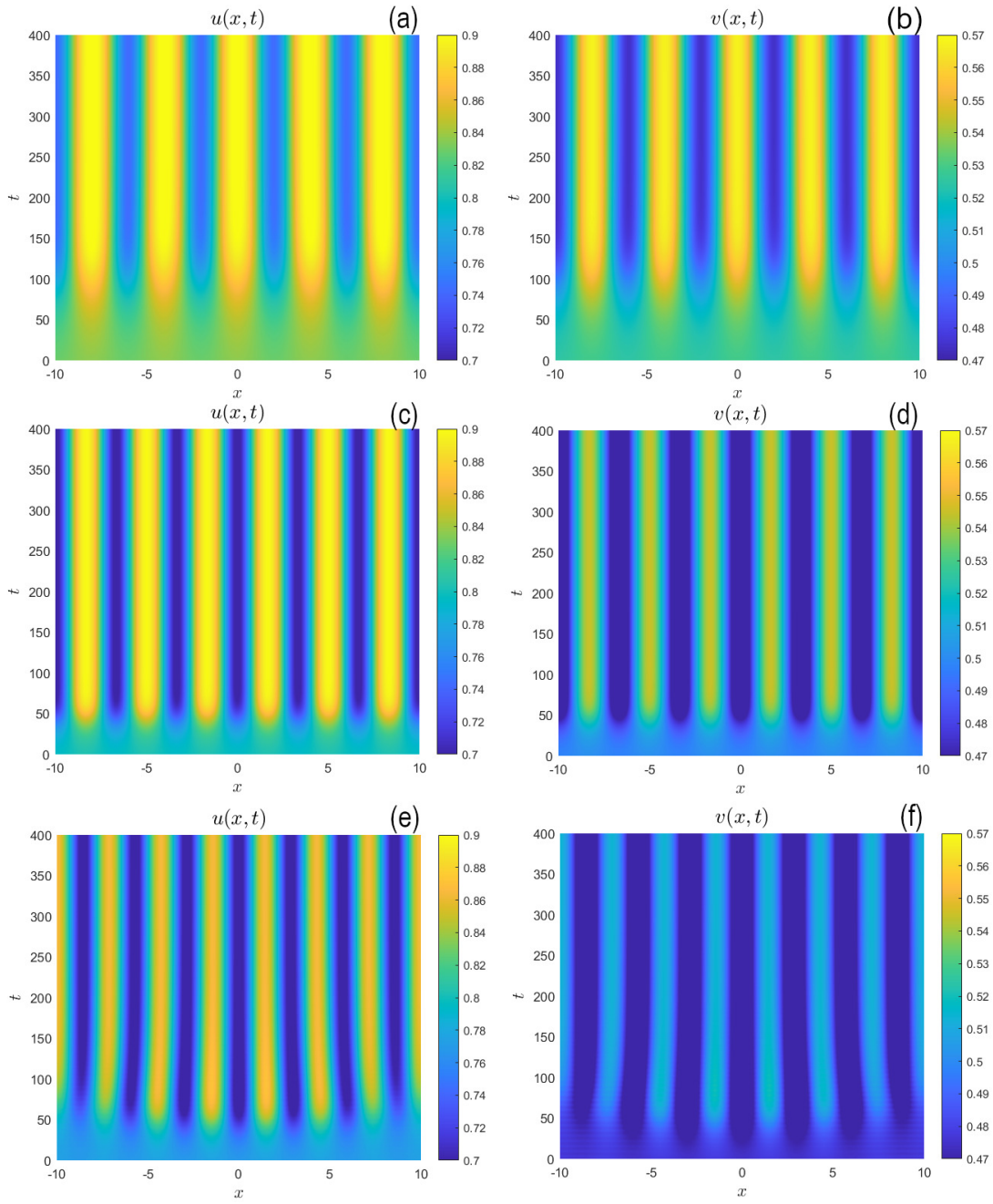

Figure 4. Spatio-temporal evolution of corrosive and passivating species obtained for different values of the control parameter d: (a),(b) $d = 1.41$; (c),(d) $d = 1.50$, and (e),(f) $d = 1.53$. They correspond to the stationary patterned branches represented in blue, green, and magenta, respectively, in Figure 3. The parameter set is the same as in Figure 2.

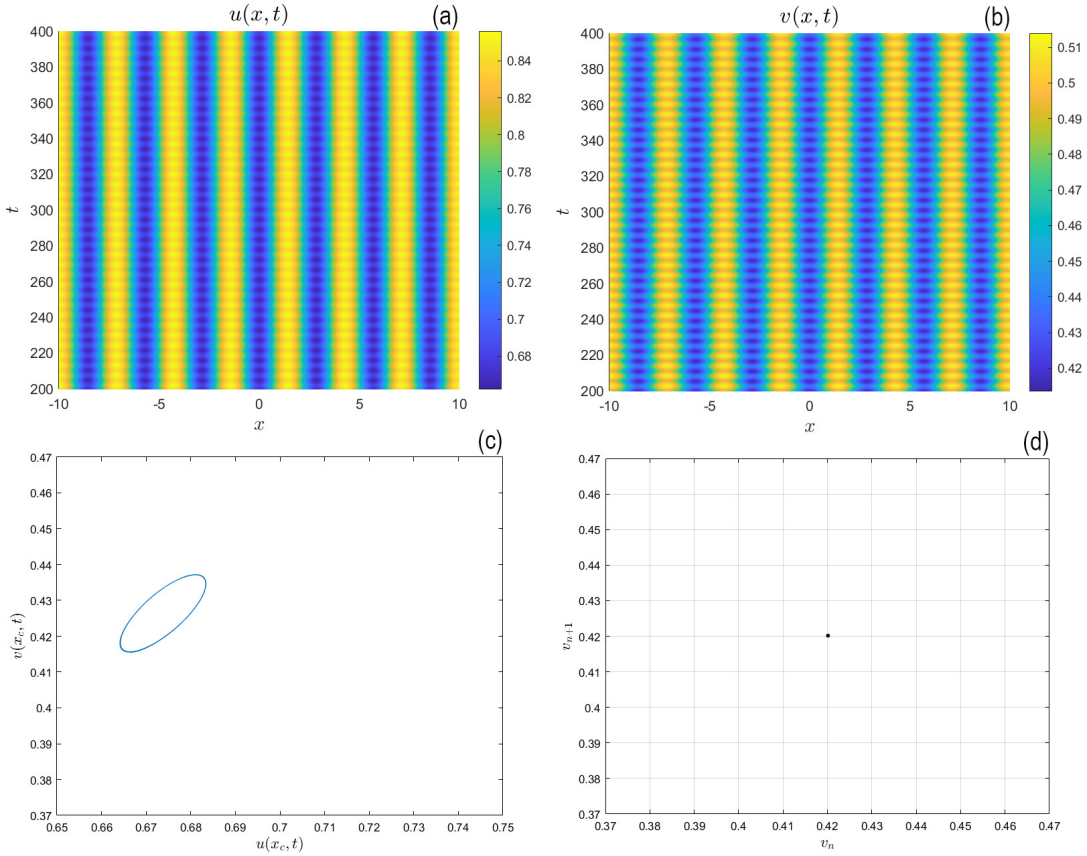

Figure 5. Oscillatory patterned dynamics in a 1D domain resulting from the superposition of Turing and Hopf branches. (a),(b) Spatio-temporal evolution of corrosive and passivating species obtained for $d = 1.69 > d_H$. This corresponds to an oscillatory patterned solution given by the superposition of the Turing and Hopf branches depicted in magenta and orange, respectively, in Figure 3. The parameter set is the same as in Figure 2. (c) Phase portrait depicting the resulting system's trajectory in the (u, v) plane evaluated at the middle point of the computational domain $x = x_c = 0$. (d) The corresponding Poincarè map.

Finally, note that other bifurcating branches have been intentionally omitted from the plot as they are inherently unstable and do not add relevant contribution to our analysis.

To validate the above predictions, we integrate the proposed model Eq (2.11) numerically in the 1D case in a MATLAB [15] environment. Neumann boundary conditions are applied to simulate zero-flux conditions at the edges of the domain $x = \pm 10$. The initial condition is in the form of a small spatially-periodic perturbation of the steady state, where the wavelength is typically extracted from the continuation analysis. We develop an implicit finite-difference scheme, in which the reaction terms and the transport terms are treated implicitly. For details on the numerical method used, see [15].

First, in Figure 4 we report the spatio-temporal evolution of the corrosive $u(x, t)$ and the passivating $v(x, t)$ densities obtained when the control parameter is in the range $d_T < d < d_H$. As an illustrative example, to mimic the stable branches depicted in blue, green, and magenta, respectively, in Figure 3, we choose $d = 1.41$ (panels (a),(b)), $d = 1.50$ (panels (c),(d)), and $d = 1.53$ (panels (e),(f)). As it can be noticed, results agree satisfactorily well with our predictions and with results of continuation anal-

ysis. In fact, once the steady-state $\mathbf{E}_3^*$ is destabilized by a non-homogeneous perturbation, it converges toward stable spatially-periodic stationary patterned states. With the increase in the control parameter, the solutions are characterized by progressively decreasing wavelengths and amplitudes, in line with Figure 3. This spontaneous spatial symmetry breaking reflects, from the chemical viewpoint, the formation of alternating cathodic (areas protected by the passive film) and anodic zones (high concentration of corrosive species), the last of which act as a classic precursor to the localized corrosion or *pitting* observed, for instance, in the bottom of fuel tanks [5, 10, 12, 13, 15]. In particular, the increase in the number of corrosion bands is accompanied by a decrease in their thickness, demonstrating that the morphology of the corrosion patterns can be strongly modulated by the carrying capacity of the passivating species. Indeed, increasing values of d enables us to mimic a reduction of the corrosion strength, so that the emerging patterns are more spatially confined.

When the control parameter overcomes the Hopf threshold d_H, the system is expected to enter a different regime. As proven in Figure 5, which is obtained for $d = 1.69 > d_H$, a stable spatially-periodic oscillatory-in-time solution emerges (see panels (a),(b)), an indication of the superposition of Turing and Hopf instabilities. For this value of the control parameter, stable Turing (magenta line in Figure 3) and Hopf (orange line in Figure 3) branches coexist. The analysis of phase portraits (panel (c)) and the Poincaré map (panel (d)) confirms the existence of a stable limit cycle, indicating that the system's trajectory, evaluated at a given location of the computational domain (the middle point $x = x_c = 0$ in the figure), evolves along a closed periodic trajectory in the phase space [37]. From the chemical viewpoint, the system undergoes a shift into a cyclic "breakdown-repassivation" process: The local accumulation of corrosive species u triggers the periodic rupture of the protective film v, which subsequently regenerates according to the Leslie-Gower-type recovery dynamics. Such oscillatory behavior is typically encountered in metals exposed to highly aggressive electrochemical environments, where the system constantly fluctuates between active and passive states. Experimental evidence of these oscillatory patterns have also been reported in several electrochemical studies in the literature [38].

3.2. Analyses in 2D domains

Extending the analysis to the 2D model, let us consider a square computational domain $(x, y) \in \mathbb{R}^2 : x \in [-5, 5], y \in [-5, 5]$ and build the corresponding bifurcation diagram, as shown in Figure 6. All the other parameters are the same as those used in Figures 2 and 3. For simplicity, we do not report the Hopf bifurcation branch (as no changes are expected with respect to the 1D analysis), so the analysis is restricted to the the spatial structures of patterned branches.

A first relevant result is the possibility to trigger patterns with different morphologies, such as stripes and holes, arranged in square or hexagonal matrices, as depicted in the insets of Figure 6. The emergence of holes is extremely relevant in the context of corrosion affecting the bottoms of metallic tanks storing crude oil, gasoline, biofuel, or other fuels. These sites represent areas where aggressive species (e.g., chloride ions or organic acids) disrupt the passive film, stabilized by species such as hydroxide ions, oxygen, or chemical inhibitors like nitrites and phosphates, thereby triggering localized anodic dissolution and the subsequent formation of pitting, as shown in Figure 7. In this picture, panels (a) and (b) depict extended areas (on the scale of meters) affected by numerous circular corrosion pits. The other pictures provide magnified views (tens of centimeters), revealing the presence of either almost-regularly distributed circular pits (panel (c)) or, irregular, non-circular ones (panel (d)).

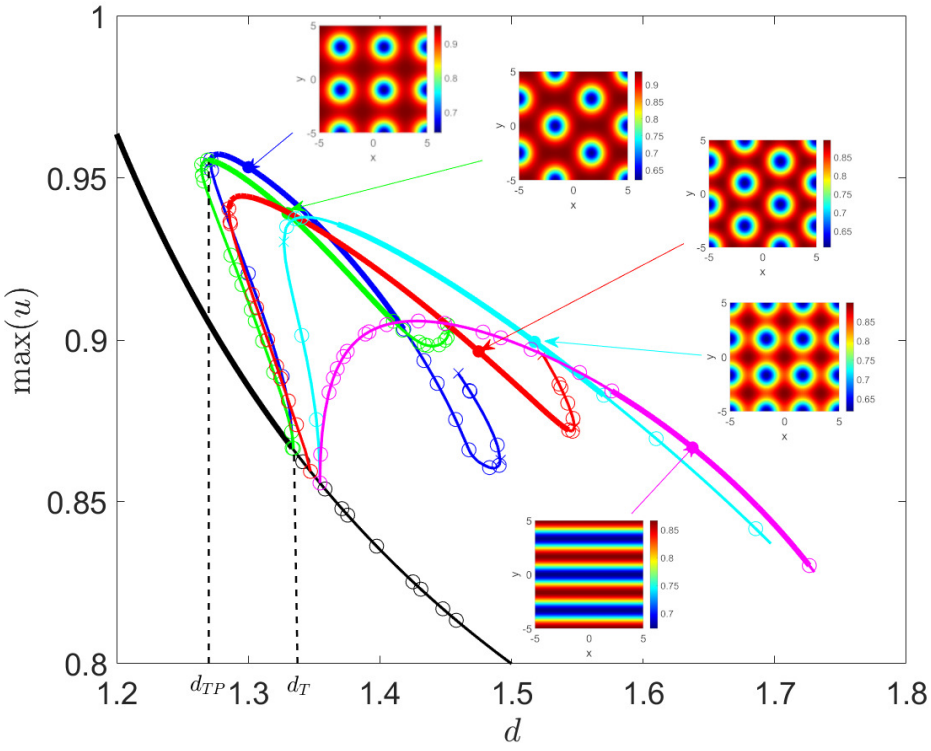

Figure 6. Bifurcation diagram for the 2D model computed with the continuation tool pde2path on a square domain $[-5, 5] \times [-5, 5]$, with d as the control parameter and $a = 1.2$. All the other parameters are the same as in Figure 2. Insets show the spatial structures for each patterned branch provided by the pde2path tool.

Moreover, comparing the 1D and 2D bifurcation diagrams highlights two noteworthy distinctions in the primary branches: A transition in their nature, from supercritical to subcritical, and a morphological change from stripes to holes. The occurrence of a subcritical instability reveals the existence of a range of the control parameter, between the turning point (d_{TP}) and the Turing threshold (d_T), where the uniform steady state and various patterned states coexist and are stable. This multistability implies that the patterned states undergo hysteresis, meaning the selected state depends on the system's history. The shift from supercritical to subcritical may be driven by several factors, including the impact of dimensionality on nonlinear feedback mechanisms near the onset of instability, the projection of nonlinearities onto domain-specific eigenfunctions, and the potential for resonance phenomena in 2D geometries. While a rigorous characterization of this transition typically requires a multiple-scale weakly-nonlinear stability analysis to derive the governing amplitude equations (see, e.g., [39]), such an investigation lies beyond the scope of this work.

To qualitatively mimic the aforementioned experimental data and to validate the results contained in the bifurcation diagram, we now perform additional investigations by integrating the full 2D governing system (2.11) numerically. We set zero-flux boundary conditions and consider initial conditions consisting of small perturbations of the steady state $\mathbf{E}_3^*$, periodic along the x and y axes.

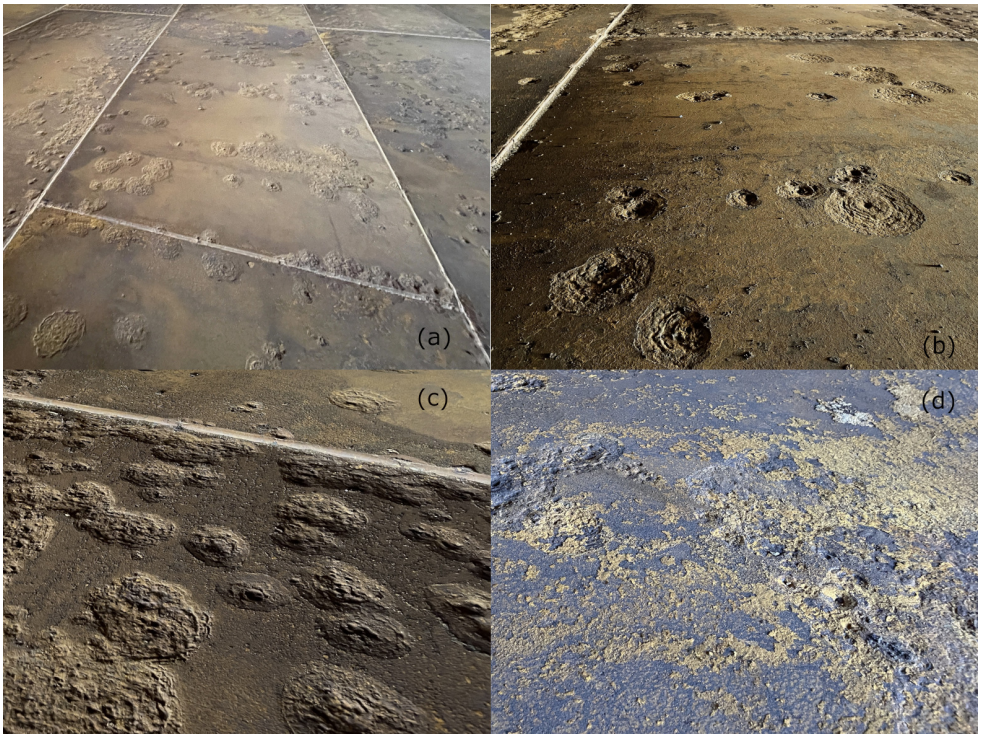

Figure 7. Experimental pictures of real corroded bottoms of fuel tanks.

The first investigation concerns the subcritical nature of the major patterned branches. The analysis is carried out by setting $d = 1.38$ initially, which represents a control parameter larger than the Turing threshold d_T. This setup originates the patterned solution reported in Figure 8(a), in the form of a square matrix of holes, that closely resembles the one obtained via pde2path (see the blue branch in Figure 6). Subsequently, this state serves as the initial condition for a new simulation in which the control parameter is decreased to $d = 1.3 < d_T$. The results shown in panel (b) reveal that the patterned configuration survives for below-threshold values, keeps the original morphology, and exhibits just a change in the amplitude. If the control parameter is further reduced to $d = 1.25$, i.e., below the turning point $d_{TP} = 1.27$, the system undergoes an abrupt transition toward the stable spatially-homogeneous steady-state (see panel (c)), confirming its subcritical nature.

Another investigation involves the possibility to initiate patterns with different morphologies, whose emergence strictly depends on the model parameters and initial configuration. Apart from regular holes distributed along a square matrix depicted in Figure 8, the system may trigger hexagons (see Figure 9(a),(b)) [39] or stripes (see Figure 9(c),(d)), agreeing with the results reported in the bifurcation diagram (Figure 6). Numerical evidence of stability is provided by the fact that these configurations persist unchanged over extended computational windows.

Furthermore, we analyze whether oscillatory behaviors can also be detected in 2D domains. To this aim, we integrate again the 2D model where we set an initial condition in the form of a stripe pattern mirroring the magenta branch in Figure 6 and increase the control parameter to $d = 1.66 > d_H$. We observe that the spatial positions of the stripes change over time within the computational domain, as illustrated in Figure 10 (panels (a)–(c)). To analyze this phenomenon more precisely, we examine the spatio-temporal evolution along the cross-section $y = 0$ (panel (d)). The resulting dynamics display an

oscillatory Turing pattern, highly analogous to the 1D case (see Figure 5(a)). To formally confirm the periodicity of this phenomenon, we track the system's trajectory in the (u, v) plane at $(x, y) = (0, 0)$. The emergence of a limit cycle is visible (panel (e)), and a distinct point results in the Poincarè map (panel (f)). These findings conclusively demonstrate that the interplay between Turing and Hopf instabilities can also manifest in 2D domains.

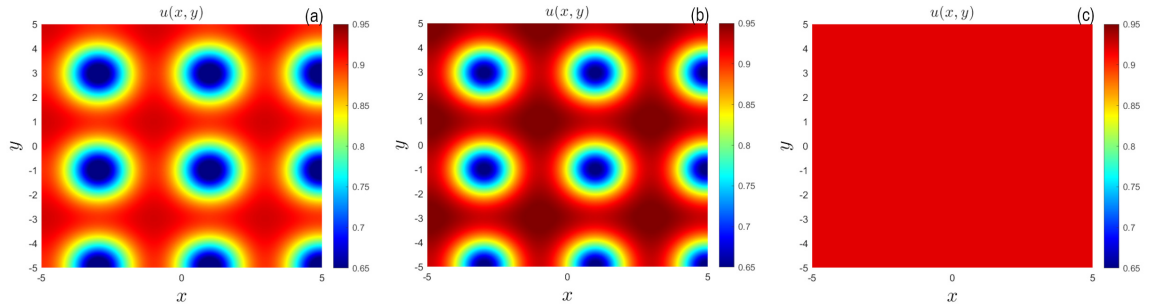

Figure 8. Results of numerical integration of the 2D model (2.11) obtained for: (a) $d = 1.38$, (b) $d = 1.3$, and (c) $d = 1.25$. The other parameters are as in Figure 2. The initial condition for (a) is a small spatially-periodic perturbation of the steady-state $\mathbf{E}_3^*$, which closely resembles the patterned configuration corresponding to the blue branch depicted in Figure 6. The steady configurations given in panels (a) and (b) are used as initial conditions for the simulations in (b) and (c), respectively.

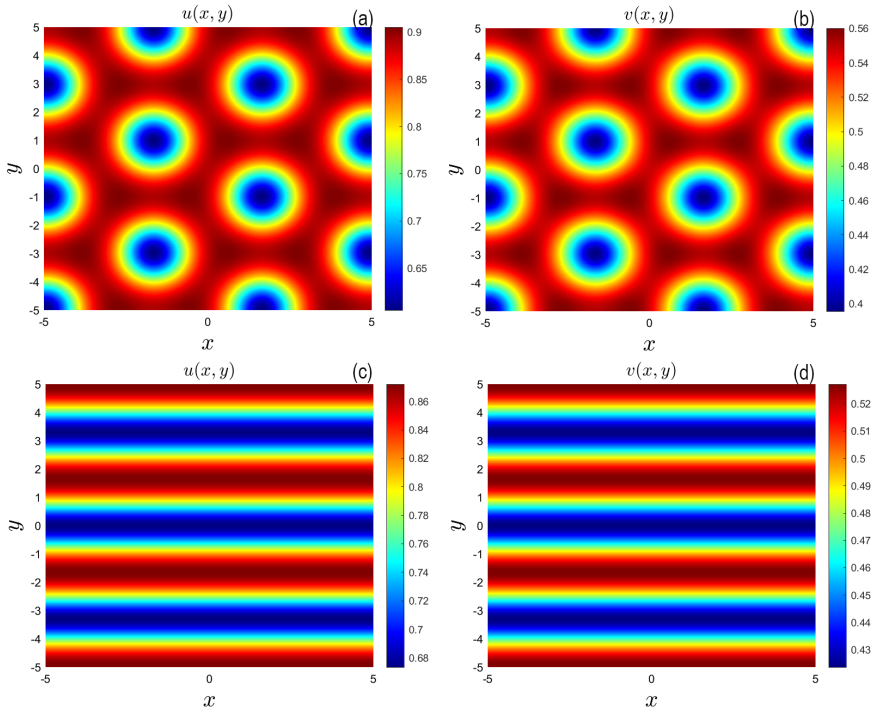

Figure 9. (a),(b) Hexagons and (c),(d) stripes obtained by integrating the 2D model (2.11) for $d = 1.50$ and $d = 1.62$, respectively. The initial conditions mirror the red and magenta branches in Figure 6. The other parameters are as in Figure 2.

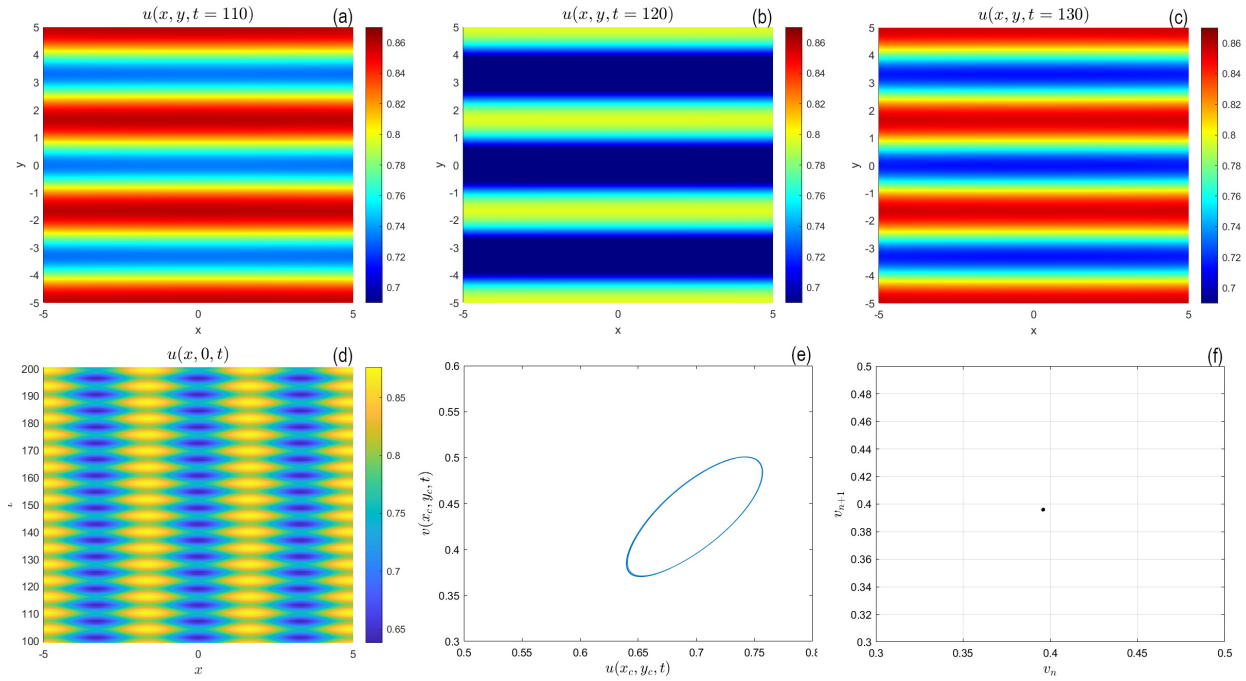

Figure 10. Oscillatory patterned dynamics in a 2D domain resulting from the superposition of Turing and Hopf branches. (a–c) Numerical integration of the 2D model over the domain $[-5, 5] \times [-5, 5]$, for $d = 1.66 > d_H$ at three time instants. The initial condition mirrors the magenta branch in Figure 6. (d) Spatio-temporal evolution in the (x, t) plane evaluated at a fixed location $y = y_c = 0$. (e) Phase portrait depicting the resulting system's trajectory in the (u, v) plane evaluated at $x = x_c = 0$. (f) The corresponding Poincarè map.

Finally, we explore pattern dynamics admitted by the proposed model over larger computational domains ($[-50, 50] \times [-50, 50]$) and larger values of the control parameter ($d \geq 1.5$). For the first simulation, we employ a small random perturbation of the steady state as initial condition. The resulting steady configurations are used as initial conditions for the subsequent ones. Starting from $d = 1.5$, we find small holes forming the so-called cold-spot patterns [40], as depicted in Figure 11 (see panel (a)). With the increase in the control parameter, at $d = 1.7$, these cold spots start coalescing and lead to mixed stripe-labyrinthine patterns (panel (b)) [40]. At $d = 2$, the structure of the pattern changes substantially and gives rise to target-like patterns [41] (panel (c)). Increasing further the control parameter, the system exhibits non-Turing patterns in the form of spiral-like patterns [41] (see panel (d) for $d = 2.5$ and (e) for $d = 3.5$). Keeping the largest value of d unchanged, doubling the side of the computational boundaries, and considering a random disturbance of the steady state as initial condition, the behavior becomes more irregular (see panel (f)).

From the perspective of corrosion phenomena, the emergence of square or hexagonal matrices of circular holes (such as those depicted in Figures 8(a),(b), 9(a),(b)), disordered cold spots (Figure 11(a)), and isolated target patterns (Figure 11(c)), qualitatively resembles the experimental circular corrosion pits shown in Figure 7(b),(c). It is evident that, while standard Turing patterns are perfectly periodic, real observations are often highly disordered. However, these configurations can be interpreted as localized structures that, initially arranged in an arbitrary non-periodic spatial pattern, destabilize and propagate their state across the background once triggered by a parameter change (e.g., a change in

the conditions of the fuel tank). Furthermore, the panels in the last row in Figure 11 could also mimic the scenario where the physical and chemical heterogeneity of an environment (such as the bottom of a fuel tank) triggers localized, irregular breakdowns in the passive film, leading to the formation of corrosion structures similar to the experimental ones depicted in Figure 7(d). This behavior finds also a mathematical counterpart in the fact that control parameter d modulates the intensity of the system's response to the corrosive species. As this coupling parameter increases, the nonlinear feedback between metal dissolution and repassivation is amplified. This strong interaction drives the system into a regime of catastrophic and unpredictable surface degradation, dominated by nonlinear fluctuations. This instability leads to a highly disordered corrosion morphology, characteristic of metals exposed to aggressive electrolytic solutions or subjected to strong anodic polarization.

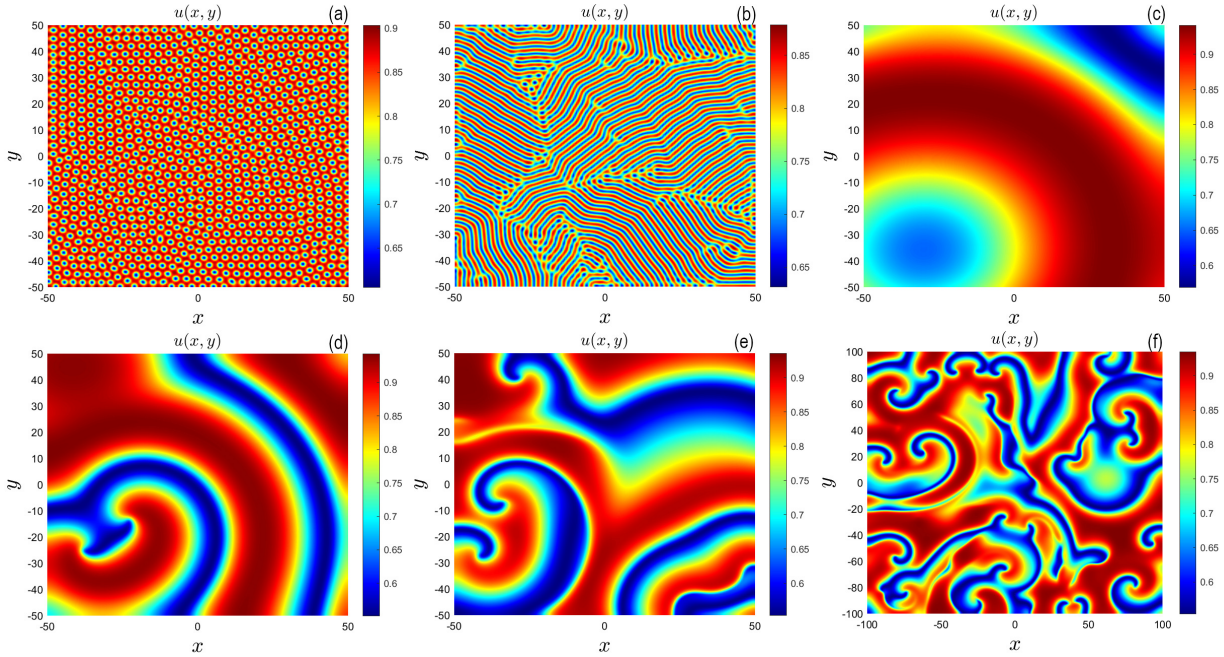

Figure 11. (a) Cold-spot, (b) mixed stripe-labyrinthine, (c) target, and (d),(e) non-Turing spiral-like patterns obtained in a computational domain $[-50, 50] \times [-50, 50]$ for $d = 1.5$, 1.7, 2.0, 2.5, and 3.5, respectively. (f) Non-Turing spiral-like patterns obtained for $d = 3.5$ in the larger computational domain $[-100, 100] \times [-100, 100]$.

4. Conclusions

In this work, we address a critical challenge introduced by the transition toward green technologies: The risks associated with the release of hazardous materials due to potential failures in managing the localized corrosion at the bottom of fuel tanks. Specifically, the proposed model is designed to characterize the critical onset of corrosion, the so-called pitting initiation phase, rather than the subsequent stages of pit growth and evolution. By focusing on this early stage, the framework captures the fundamental mechanisms that precede structural damage. Our approach relies on a two-compartment reaction-diffusion model, based on a generalized version of the Barkley model for excitable systems, to describe the concentrations of corrosive and passivating species. While preserving the original Allee

kinetics for the corrosive species, the model introduces a logistic-like law for the passivating species featuring a corrosive-dependent carrying capacity. This formulation can be classified as Leslie-Gower dynamics with a Holling type II functional response. This modified kinetics addresses the oversimplifications of the original Barkley model by accounting for the phenomenological observation that the repassivation rate and the stability of the passive film are dynamically influenced by the corrosive environment.

Through rigorous analytical and numerical investigations, several key features of the model are highlighted.

Analytically, the boundedness of solutions and the emergence of Hopf bifurcations in the associated dynamical system are first established. Subsequently, a linear stability analysis of the full spatial model identifies the conditions for Turing instability. The plot of the instability regions reveals a broad parameter space where stationary and oscillatory corrosion patterns may emerge. Notably, compared to previous corrosion models [15], this framework yields the advantage of initiating corrosion patterns without requiring cross-diffusion effects.

Numerically, integrating the governing system and applying continuation techniques across 1D and 2D domains provides deep insights into the system's behavior. These simulations reveal a remarkable morphological variety of patterns, including stripes, holes, labyrinths, targets, and non-Turing spiral-like structures. The emergence of target, holes, and spiral-like patterns is particularly relevant, as it qualitatively captures the pitting phenomenon experimentally observed at the bottom of real fuel tanks. The system also exhibits a sensitivity to spatial dimensionality, shifting from a supercritical regime in 1D to a subcritical behavior in 2D domains. This subcritical regime implies the presence of hysteresis, indicating that corrosion damage can persist even when the control parameter drops below the critical threshold. Furthermore, numerical investigations corroborate the theoretical predictions, demonstrating that stationary and oscillatory Turing patterns can emerge in 1D and 2D domains, with the oscillatory behaviors driven by the coexistence of Turing and Hopf instabilities.

Future developments of this work may proceed along three major directions. First, inspired by the literature [15], the inclusion of an additive cross-diffusion term could be investigated. Chemically, this transport mechanism would model the active migration of passivating species toward zones of high corrosive concentration, thereby simulating a dynamic material protection mechanism. Second, following [13], the model could benefit from a third differential equation describing the spatio-temporal growth of corrosion pits across the metal surface. Third, in line with [42–44], the model parameters could explicitly account for the intrinsic and spatial heterogeneity of the environment. This would naturally break the symmetry of the system, leading to imperfect, patchy patterns that would capture, more accurately, the disordered states shown in the observations. Such extensions would contribute to develop a more robust framework for analyzing pitting initiation and evolution, aiding the safety management of fuel tanks.

Author contributions

Giancarlo Consolo: Writing – review & editing, Writing – original draft, Supervision, Software, Methodology, Investigation, Funding acquisition, Formal analysis, Conceptualization. Guglielmo Inferrera: Writing – review & editing, Writing – original draft, Software, Methodology, Investigation, Formal analysis.

Use of AI tools declaration

The authors declare they have not used Artificial Intelligence (AI) tools in the creation of this article.

Acknowledgments

This research was funded by MUR (Italian Ministry of University and Research) PNRR Missione 4, Componente 2, Investimento 1.1–Bando Prin 2022, Decreto Direttoriale no. 104 del 02-02-2022, through PRIN2022 Project PRIN202248TY47 "Modelling complex biOlogical systeMs for biofuEl productioN and sTorAge: mathematics meets green industry (MOMENTA)", CUP J53D23003580006, and by INdAM-GNFM. The authors gratefully acknowledge prof. Edoardo Proverbio and the anonymous referees for their valuable comments and suggestions.

Conflict of interest

The authors declare that they have no known competing financial interests or personal relationships that could have appeared to influence the work reported in this paper.

References

1. *American Petroleum Institute, API Standard 650, 13th edition*. Available from: https://www.api.org/products-andservices/standards/important-standards-announcements/standard650.
2. N. Perez, Electrochemical corrosion, in *Electrochemistry and Corrosion Science*, Springer International Publishing, Cham, (2016), 1–23. https://doi.org/10.1007/978-3-319-24847-9-1
3. D. A. Shifler, Localized corrosion, in *Corrosion in Marine Environments*, John Wiley & Sons, Inc., (2022), 63–121. https://doi.org/10.1002/9781119788867.ch4
4. J. R. Galvele, Pitting corrosion, in *Treatise on Materials Science and Technology*, Elsevier, (1983), 1–57. https://doi.org/10.1016/B978-0-12-633670-2.50006-1
5. M. F. Milazzo, G. Ancione, P. Bragatto, E. Proverbio, A probabilistic approach for the estimation of the residual useful lifetime of atmospheric storage tanks in oil industry, *J. Loss Prev. Process Ind.*, **77** (2022), 104781. https://doi.org/10.1016/j.jlp.2022.104781
6. L. N. Komariah, S. Arita, B. E. Prianda, T. K. Dewi, Technical assessment of biodiesel storage tank: A corrosion case study, *J. King Saud Univ. Eng. Sci.*, **35** (2023), 232–237. https://doi.org/10.1016/j.jksues.2021.03.016
7. A. Capuozzo, A. Tenore, F. Russo, L. Frunzo, A double free boundary problem on microbially induced corrosion in wastewater concrete, *Math. Eng.*, **7** (2025), 481–504. https://doi.org/10.3934/mine.2025020
8. *American Petroleum Institute, API 580 - Risk Based Inspection*, 2023. Available from: https://www.api.org/products-andservices/individual-certification-programs/certifications/api580.
9. *Engineering Equipment and Materials Users Association, EEMUA Publication 159 Digital*. Available from: https://www.eemua.org/Products/Publications/Digital/EEMUA-Publication-159.aspx.

10. H. Moradi, G. Grifò, M. F. Milazzo, E. Proverbio, G. Consolo, Modelling localized corrosion in biofuel storage tanks, *Math. Biosci. Eng.*, **22** (2025), 677–699. https://doi.org/10.3934/mbe.2025025
11. C. Cui, R. Ma, E. Martínez-Pañeda, Electro-chemo-mechanical phase field modeling of localized corrosion: Theory and COMSOL implementation, *Eng. Comput.*, **39** (2023), 3877–3894. https://doi.org/10.1007/s00366-023-01833-8
12. P. Carbone, E. Piperopoulos, G. Consolo, M. F. Milazzo, Modelling corrosion of atmospheric storage tanks to support the safety management, *Chem. Eng. Trans.* (in press).
13. B. C. Batista, E. Romanovskaia, V. Romanovski, M. Emmanuel, J. T. Burns, J. Ma, et al., Morphogenic modeling of corrosion reveals complex effects of intermetallic particles, *Adv. Sci.*, **11** (2024), 2404986. https://doi.org/10.1002/advs.202404986
14. A. Pollino, On the modeling of wave phenomena in pit corrosion, *Ric. Mat.*, **74** (2025), 2727–2739. https://doi.org/10.1007/s11587-025-00970-0
15. G. Consolo, G. Inferrera, E. Proverbio, C. Soresina, An extended corrosive-passivating model with cross-diffusion for the initiation of corrosion patterns, *Physica D*, **483** (2025), 134986. https://doi.org/10.1016/j.physd.2025.134986
16. D. Barkley, A model for fast computer simulation in excitable media, *Physica D*, **49** (1991), 61. https://doi.org/10.1016/0167-2789(91)90194-E
17. D. Barkley, Euclidean symmetry and the dynamics of rotating spiral waves, *Phys. Rev. Lett.*, **72** (1994), 164. https://doi.org/10.1103/PhysRevLett.72.164
18. A. Turing, The chemical basis of morphogenesis, *Philosoph. Trans. Royal Soc. B*, **237** (1952), 37–72. https://doi.org/10.1007/BF02459572
19. J. D. Murray, *Mathematical Biology II: Spatial Models and Biomedical Applications*, 3rd edition, Interdisciplinary Applied Mathematics, New York: Springer-Verlag, 2003. https://doi.org/10.1007/b98869
20. M. A. Aziz-Alaoui, M. D. Okiye, Boundedness and global stability for a predator-prey model with modified Leslie-Gower and Holling-type II schemes, *Appl. Math. Lett.*, **16** (2003), 1069–1075. https://doi.org/10.1016/S0893-9659(03)90096-6
21. C. Zhang, X. Li, Dynamics of a discrete Leslie–Gower model with harvesting and Holling-II functional response, *Mathematics*, **11** (2023), 3303. https://doi.org/10.3390/math11153303
22. N. DeTal, A. Kaboudian, F. H. Fenton, Terminating spiral waves with a single designed stimulus, *Proc. Natl. Acad. Sci. U.S.A.*, **119** (2022), e2117568119. https://doi.org/10.1073/pnas.2117568119
23. K. Gallagher, M. A. Strobl, D. S. Park, F. C. Spoendlin, R. A. Gatenby, P. K. Maini, et al., Mathematical model-driven deep learning enables personalized adaptive therapy, *Cancer Res.*, **84** (2024), 1929. https://doi.org/10.1158/0008-5472.CAN-23-2040
24. D. D. Macdonald, The point defect model for the passive state, *J. Electrochem. Soc.*, **139** (1992), 3434. https://doi.org/10.1149/1.2069096
25. M. Xing, M. He, Z. Li, Dynamics of a modified Leslie-Gower predator-prey model with double Allee effects, *Math. Biosci. Eng.*, **21** (2024), 792–831. https://doi.org/10.3934/mbe.2024034

26. P. Salehikahrizsangi, K. Raeissi, F. Karimzadeh, L. Calabrese, E. Proverbio, Effects of surface morphology on erosion–corrosion and corrosion resistance of highly hydrophobic nickel–tungsten electrodeposited film, *Coatings*, **11** (2021), 1084. https://doi.org/10.3390/coatings11091084

27. J. Smoller, *Shock Waves and Reaction–Diffusion Equations*, 2nd edition, Springer, 1994. https://doi.org/10.1007/978-1-4612-0873-0

28. G. Consolo, C. Curró, G. Grifó, G. Valenti, Vegetation pattern formation and transition in dryland ecosystems with finite soil resources and inertia, *Physica D*, **476** (2025), 134601. https://doi.org/10.1016/j.physd.2025.134601

29. G. Consolo, C. Curró, G. Grifó, G. Valenti, Stationary and oscillatory patterned solutions in three-compartment reaction–diffusion systems: Theory and application to dryland ecology, *Chaos, Solitons Fractals*, **186** (2024), 115287. https://doi.org/10.1016/j.chaos.2024.115287

30. D. Lacitignola, I. Sgura, B. Bozzini, Turing-Hopf patterns in a morphochemical model for electrodeposition with cross-diffusion, *Appl. Eng. Sci.*, **5** (2021), 100034. https://doi.org/10.1016/j.apples.2020.100034

31. G. Schneider, H. Uecker, *Nonlinear PDEs: A Dynamical Systems Approach*, Graduate Studies in Mathematics, American Mathematical Society, Providence, RI, 2017. https://doi.org/10.1090/gsm/182

32. H. Uecker, Hopf bifurcation and time periodic orbits with pde2path–algorithms and applications, *Commun. Comput. Phys.*, **25** (2019), 812–852. https://doi.org/10.4208/cicp.OA-2017-0181

33. H. Uecker, *Numerical Continuation and Bifurcation in Nonlinear PDEs*, Philadelphia: Society for Industrial and Applied Mathematics (SIAM), 2021. https://doi.org/10.1137/1.9781611976618

34. L. S. Tuckerman, D. Barkley, Bifurcation analysis of the Eckhaus instability, *Physica D*, **46** (1990), 57–86. https://doi.org/10.1016/0167-2789(90)90113-4

35. J. P. Eckmann, T. Gallay, C. E. Wayne, Phase slips and the Eckhaus instability, *Nonlinearity*, **8** (1995), 943–961. https://doi.org/10.1088/0951-7715/8/6/004

36. G. Consolo, G. Grifó, Eckhaus instability of stationary patterns in hyperbolic reaction–diffusion models on large finite domains, *Partial Differ. Equations Appl.*, **3** (2022), 57. https://doi.org/10.1007/s42985-022-00193-0

37. V. Giunta, M. C. Lombardo, M. Sammartino, Pattern formation and transition to chaos in a chemotaxis model of acute inflammation, *SIAM J. Appl. Dyn. Syst.*, **20** (2021), 1844–1881. https://doi.org/10.1137/20M1358104

38. D. Sazou, M. Pavlidou, M. Pagitsas, Potential oscillations induced by localized corrosion of the passivity on iron in halide-containing sulfuric acid media as a probe for a comparative study of the halide effect, *J. Electroanal. Chem.*, **675** (2012), 54–67. https://doi.org/10.1016/j.jelechem.2012.04.012

39. G. Grifó, G. Consolo, C. Curró, G. Valenti, Rhombic and hexagonal pattern formation in 2D hyperbolic reaction–transport systems in the context of dryland ecology, *Physica D*, **449** (2023), 133745. https://doi.org/10.1016/j.physd.2023.133745

40. M. Banerjee, S. Ghorai, N. Mukherjee, Study of cross-diffusion induced Turing patterns in a ratio-dependent prey-predator model via amplitude equations, *Appl. Math. Model.*, **55** (2018), 383–399. https://doi.org/10.1016/j.apm.2017.11.005

41. G. Wang, Q. Wang, P. He, S. Pullela, M. Marquez, Z. Cheng, Target-wave to spiral-wave pattern transition in a discrete Belousov–Zhabotinsky reaction driven by inactive resin beads, *Phys. Rev. E*, **82** (2010), 045201. https://doi.org/10.1103/PhysRevE.82.045201

42. H. Yizhaq, S. Sela, T. Svoray, S. Assouline, G. Bel, Effects of heterogeneous soil–water diffusivity on vegetation pattern formation, *Water Resour. Res.*, **50** (2014), 5743–5758. https://doi.org/10.1002/2013WR015158

43. G. Bel, A. Hagberg, E. Meron, Aperiodic clustered and periodic hexagonal vegetation spot arrays explained by inhomogeneous environments and climate trends in arid ecosystems, *Theor. Ecol.*, **5** (2012), 321–331. https://doi.org/10.1007/s12080-012-0163-6

44. D. Pinto-Ramos, S. Echeverría-Alar, M. G. Clerc, M. Tlidi, Vegetation covers phase separation in inhomogeneous environments, *Chaos, Solitons Fractals*, **163** (2022), 112518. https://doi.org/10.1016/j.chaos.2022.112518

AIMS Press